Journal of Applied Crystallography

ISSN 1600-5767

Electron-density analysis of halide · · · halide through-space magnetic exchange

Rebecca Scatena,^a* Zachary E. Manson,^b Jamie L. Manson,^b David R. Allan,^a Paul A. Goddard^c and Roger D. Johnson^{a,d,e}

^aDiamond Light Source, Rutherford Appleton Laboratory-STFC, Chilton, Didcot OX11 0QX, United Kingdom, ^bDepartment of Chemistry and Biochemistry, Eastern Washington University, Cheney, Washington 99004 USA, ^cDepartment of Physics, University of Warwick, Gibbet Hill Road, Coventry, CV4 7AL United Kingdom, ^dDepartment of Physics and Astronomy, University College London, Gower Street, London WC1E 6BT, United Kingdom, and ^eLondon Centre for Nanotechnology, University College London, Gower Street, London WC1E 6BT, United Kingdom. Correspondence e-mail: rebecca.scatena@diamond.ac.uk

We present a combined experimental and density functional theory study that characterizes the charge and spin density in $[NiX_2(3,5\text{-lutidine})_4]$ [X=Cl, Br, and I]. In this material, magnetic exchange interactions occur via Ni^{2+} -halide··· halide- Ni^{2+} pathways forming one-dimensional chains. We find evidence for weak halide-halide covalency in the iodine system, which is greatly reduced when X=Br, and is absent for X=Cl; consistent with the reported 'switching-on' of magnetic exchange in the larger halide cases. Our results are benchmarked against density functional theory calculations on $[NiHF_2(pyrazine)_2]SbF_6$, in which the primary magnetic exchange is mediated by F-H-F bridging ligands. This comparison indicates that, despite the largely depleted charge density found at the centre of halide··· halide bonds, these through-space interactions can support strong magnetic exchange gated by weak covalency, and enhanced by significant electron density overlapping that of the transition metal centres.

© 0000 International Union of Crystallography

1. Introduction

Coordination polymers self-assemble from versatile 'building blocks' that span both an enormous chemical space and broad range of physical properties. Crucially, if enough is known about each component, the target material properties might be anticipated from the sum of its parts. The study of low-dimensional magnetism has especially benefited from this materials design approach, where specific magnetic properties such as anisotropy or dimensionality have been designed from the outset, or the Hamiltonian parameters of a particular quantum model of interest have been fine tuned [1–3].

The majority of coordination-polymer quantum magnets are based on transition-metal (TM) magnetic centres that interact via nearest-neighbour magnetic exchange mediated by the molecular orbitals of organic bridging ligands such as formate [4,5], pyrazine [6,7], or pyrimidine [8,9]. However, fundamental details of the interactions remain a topic of debate. This issue is especially pertinent in understanding how to increase the strength of magnetic exchange interactions in coordination-polymer quantum magnets with a view to application in devices. For example, it has been suggested that exchange could be enhanced by engaging π -orbitals of aromatic rings [10], which

provide a continuous electron density spanning the whole bridging ligand. Alternatively, it may be that molecular orbitals with electron density depleted in the centre of the ligand, but bunched towards the binding site, give rise to the strongest interactions on account of the larger overlap with the TM orbitals [4]. These opposing theories come into the spotlight when seemingly impossible magnetic exchange is mediated *through-space* between non-bridging ligands.

In $[NiX_2(3,5-lutidine)_4]$ [X=Cl, Br, and I], Ni^{2+} ions are octahedrally coordinated with four equatorial 3,5-lutidine neutral ligands and two apical X^- anions (Figure 1a). Ni^{2+} is a $3d^8$ S=1 ion, and in this coordination one anticipates fully occupied (non-magnetic) t_{2g} orbitals and half occupied e_g orbitals. The ion is therefore not Jahn-Teller active, and superexchange interactions may occur via all coordinating ligands. The compound crystallises in a well-ordered tetragonal crystal structure (space group $P^4_n nc$) composed of interleaved $[NiX_2(3,5-lutidine)_4]$ units (Figures 1b and 1c) forming staggered layers, with opposing $X \cdots X$ ions spanning an entire layer (Figure 1c). For X = Cl, Br, and I long-range magnetic order has not been observed down to the lowest measured temperatures [11,12]. However, the temperature and field dependence of the

1

¹ Deceased 7 June 2023

magnetic susceptibility clearly indicated one-dimensional magnetic correlations in the Br and I samples at low temperature, which based on the atomic connectivity must be associated with through-space magnetic exchange along $-\text{Ni}^{2+}$ - $\text{X} \cdot \cdot \cdot \times \text{Ni}^{2+}$ -chains. Analysis of the magnetic susceptibility data gave antiferromagnetic Heisenberg exchange coefficients (J) of ~ 0 , 0.8(1), 17.5(1) K for X = Cl, Br, and I, respectively [11, 12], demonstrating a dramatic 'switching-on' of magnetic exchange in samples with larger halide anions. Furthermore, values for the single-ion-anisotropy parameter, D, were found to be 9.6(7), 6.1(5), and -1.2(3) K for X = Cl, Br, and I, respectively, where negative D corresponds to easy-axis anisotropy parallel to the crystallographic c-axis [11, 12].

In this paper, we analyse both charge and spin degrees of freedom in the electron density of $[NiX_2(3,5-lutidine)_4]$, with X = Cl, Br, and I, in order to understand the nature of magnetic exchange via through-space Ni²⁺-halide··· halide-Ni²⁺ interactions. We note that this approach has proven successful in providing critical insight into the nature of exchange mediated by bridging ligands in coordination polymers [4–6, 13, 14]. We establish highly accurate empirical crystal structures using single-crystal synchrotron X-ray diffraction and Hirshfeld atom refinement (HAR). These structures are then used in density functional theory (DFT) calculations to determine the electron density for all three materials. The superior diffraction data obtained from the iodine compound permitted experimental determination of the charge density, which we use to confirm the validity of the DFT results. We benchmark our analysis of the chemical bonding in $[NiX_2(3,5-lutidine)_4]$ against calculations on the well-studied compound, [NiHF₂(pyrazine)₂]SbF₆, in which the strongest magnetic exchange is mediated via F-H-F bridging ligands [15]. We show evidence for weak halidehalide covalency in the iodine compound, which facilities relatively strong magnetic exchange despite a largely depleted charge density at the centre. Our results suggest that throughspace interactions in coordination polymers could facilitate very strong exchange interactions as they naturally result in charge density predominantly overlapped with the transition metal centres, so long as they are close enough to establish even a small degree of covalency.

2. Methods

2.1. Synthesis

Single crystals of $[NiX_2(3,5\text{-lutidine})_4]$ with approximate dimensions $5\times5\times5$ microns (X=Cl,Br) and $100\times100\times100$ microns (X=I) were synthesised following the procedures described in [11,12]. Single crystals of $[NiHF_2(pyrazine)_2]SbF_6$ with dimensions $100\times100\times100$ microns were synthesised following the procedure described in the Supplemental Material of [15].

2.2. X-ray diffraction

X-ray diffraction data were collected at beamline I19 at Diamond Light Source using the fixed- χ 3-circle diffractometer equipped with a Pilatus 2M detector and Oxford Cryostream

flow cryostat [16]. The X-ray energy was set to the Zr K edge to have a wavelength of 0.68890 Å. As-grown single crystals samples were mounted on kapton loops. Redundant data sets up to 0.40 Å resolution (Appendix A) were collected at 100(2) K for all samples. Standard data sets [17] were collected carrying out a 360 $^{\circ}$ Φ -scan at 2θ position 0 using 0.002% and 1% beam transmission to collect accurate Bragg reflections and thermal diffuse scattering respectively in the 100 - 300 K range in steps of 0.1 $^{\circ}$.

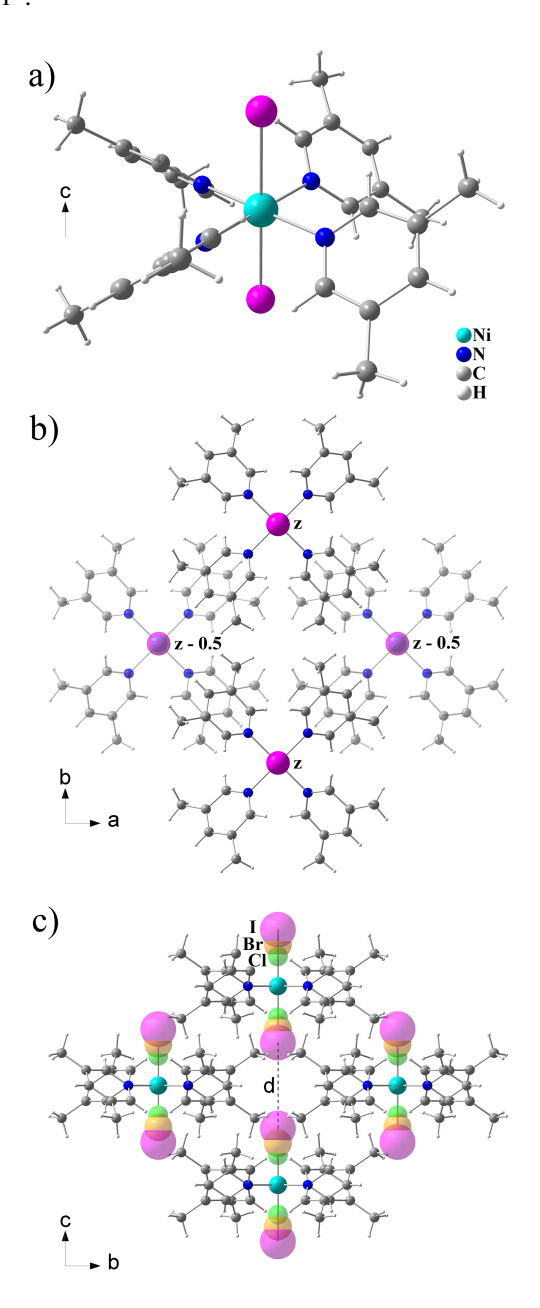


Figure 1 Crystal structure of $[NiX_2(3,5-lutidine)_4]$ a) highlighting the coordination of Ni^{2+} centres, and a single unit cell viewed b) down the *c*-axis and c) viewed down the *a*-axis. X = Cl, Br, and I anions are superposed in (c) using green, yellow, and purple spheres, respectively.

Integration, scaling and correction for Lorentz polarization

and absorption of the data were carried out using the Dials routines implemented in Xia2 [18]. Reconstruction of reciprocal space planes were obtained using CrysAlisPro software [19].

For all samples, independent atom models (IAM) were refined against the X-ray diffraction data using olex2.refine in Olex2 [20]. The obtained structural models were then used as a starting point for HAR using NoSperaA2 [21] and Orca [22], as implemented Olex2. For this refinement the asymmetric unit was expanded to a [NiX $_2$ (3,5-lutidine) $_4$] cluster and calculated at the R2SCAN/def2-TZVP level of theory using the triplet configuration and a slow convergence criterion.

For [NiI₂(3,5-lutidine)₄] the Hansen–Coppens multipolar model [23] was refined in XD2016 [24]. Isotropic extinction was estimated according to the Becker-Coppens equation [25]. All multipoles up to hexadecapoles, and contraction and expansion parameters κ and κ' , were refined for all non-hydrogen atoms. Independent sets of κ and κ' were refined for different elements. Anharmonic motion up to the fourth-order was refined only for Cu and I atoms, whereas second order anisotropic thermal parameters were refined for all other non-H atoms. Hydrogen atoms were also described aspherically by refining a dipole along their bond. The hydrogen κ and κ' parameters were constrained to the standard value of 1.2. Selected crystallographic data and refinement details are summarized in Table 1, and a residual density analysis is shown in Figure 4 of Appendix A. Topological properties of the electron density and integrated atomic charges were calculated using the XDPROP module of XD2016 software, shown in Figure 5 of Appendix A. This analysis was not possible for the X = Cl or Br materials, as beam damage to these smaller samples under prolonged exposure prevented data collection with sufficiently high statistics. Hydrogen positions were set to theoretical distances using the hydrogen riding model, and isotropic thermal parameters were refined for all hydrogen atoms.

2.3. Density functional theory

The experimental geometries obtained from HAR refinement were used in all DFT calculations. The energy difference between ferromagnetic (FM) and antiferromagnetic (AFM) spin configurations along the Ni²⁺-X···X-Ni²⁺ or Ni²⁺-FHF-Ni²⁺ pathways was calculated using CRYSTAL23 [26] with the B3LYP functional and POB-TZVP-REV2 basis set. The energy difference was converted into Heisenberg exchange coefficients (J) according to a single-J convention using the following relationship:

$$J = \frac{E_{AFM} - E_{FM}}{N \times S(2S+1)} \tag{1}$$

where N is the number of exchange interactions in the unit cell and S is the total atomic spin. Spin-density distribution maps were obtained using the property module of CRYSTAL23. The electron density of $Ni_2X_4(3,5\text{-lutidine})_8$ and $Ni_2(HF_2)_3(pyrazine)_8$ clusters, which include the complete superexchange pathway between Ni^{2+} ions, was calculated with Gaussian16 using 6-311G(d,p) basis set with B3LYP and wB97XD functionals. Chemical-bonding analysis was carried out with the quantum theory of atoms in molecules (QTAIM)

[27] as implemented in AIMQB [28] using a fine IAS mesh and the 'auto' integration radius.

3. Results and Discussion

3.1. Crystal structures

X-ray diffraction experiments at 100 K provided high-quality data for all samples up to at least 0.6 Å resolution, with the final structural models obtained by HAR refinement (Appendix A). For the investigated materials this approach gives bond lengths that are very similar to those obtained by standard refinement techniques for all atoms but hydrogen, as expected.

Table 1 reports selected inter-atomic distances in the $[NiX_2(3,5-lutidine)_4]$ and $[NiHF_2(pyrazine)_2]SbF_6$ materials. Surprisingly, the distance between Ni²⁺ ions along the chains varies only slightly on halide substitution, and is in fact inversely proportional to the halide radius. This result implies that the space-filling lutidine scaffold fixes the the Ni-Ni distance, to good approximation. As a result, as the Ni-X distances increase with the size of the halide, the X-X distances become shorter. We note that while the I-I distance is still larger than the sum of the iodine van der Waals radii, it is smaller than the sum of their anionic radii [29]. For Cl and Br the X-X distances are larger than the sum of their van der Waals radii and ionic radii. By comparison, the Ni²⁺-FHF-Ni²⁺ pathway in [NiHF₂(pyrazine)₂]SbF₆ is much shorter, with the F⁻-F⁻ distance (including the bonded H atom) being approximately half the I-I distance in [NiX₂(3,5-lutidine)₄]. Similarities can be found in the TM-halide bond lengths, but these distances alone indicate an altogether different scenario of magnetic exchange in $[NiX_2(3,5-lutidine)_4]$ and $[NiHF_2(pyrazine)_2]SbF_6$, where in the latter strong chemical interactions are expected within the exchange pathway mediated by a single molecular ligand. Remarkably, however, similar values of exchange coefficients are found for Ni²⁺-I···I-Ni²⁺ and Ni²⁺-F-H-F-Ni²⁺ interactions (Table 4). Importantly, the electronic properties of the equatorial ligands lutidine and pyrazine are expected to be similar, being both neutral N donor 6-membered aromatic ligands. This is reflected in the similar Ni-N bond distances found for all materials, which implies that differences in the exchange coefficients are established by differences along the exchange pathway in question.

Table 1Selected bond lengths of [NiX₂(3,5-lutidine)₄] and [NiHF₂(pyrazine)₂]SbF₆, determined by HAR analysis of synchrotron X-ray diffraction data measured at 100 K. The asterisk indicates that the X-X data corresponds to a F-H bond.

	Ni-Ni (Å)	X-X (Å)	Ni-X (Å)	Ni-N (Å)
[NiHF ₂ (pyz) ₂]SbF ₆	6.4357(8)	2.2851(8)*	2.0753(4)	2.1040(3)
$NiCl_2(3,5-lut)_4$	10.5513(2)	5.6395(3)	2.4559(2)	2.1279(5)
$NiBr_2(3,5-lut)_4$	10.1909(1)	4.9256(2)	2.6326(2)	2.1254(5)
NiI ₂ (3,5-lut) ₄	9.9896(1)	4.3146(2)	2.83750(7)	2.1292(3)

3.2. Thermal diffuse scattering (X=I)

In addition to the Bragg peak intensities analysed in the previous section, significant and highly textured thermal diffuse scattering (TDS) intensity was observed in the $[NiX_2(3,5-lutidine)_4]$ single-crystal synchrotron X-ray data. We note that the diffuse intensity was over 3 orders of magnitude weaker

than the Bragg peaks, and therefore did not affect integration of Bragg intensities within the statistical uncertainty. Here, we focus on the X = I compound as an exemplary case for which TDS was best measured on account of the larger crystal size and heavier scattering element. No diffuse scattering was observed in the data measured from [NiHF₂(pyrazine)₂]SbF₆.

Figure 2 shows X-ray scattering in the hk0 (top right) and h0l (bottom right) reciprocal lattice planes integrated over ± 0.25 reciprocal lattice units in the normal direction (the hk1 and hk2 planes are shown in Appendix B). The left hand side of each pane shows the result of TDS calculations detailed in Appendix B. In these model calculations we assumed that the phonons responsible for TDS were predominantly associated with nearest neighbour interactions between [NiX₂(3,5-lutidine)₄] rigid units, and we note that the observed rapid intensity fall-off as a function of Q is consistent with a scattering form factor of extended, rigid structural units. There are two molecules per unit cell, each with 3 degrees of freedom. Hence, we anticipate 6 eigenmodes; 3 acoustic and 3 optic phonons, where the acoustic phonons will dominate the TDS scattering at lower temperatures. Our model is based on stretch/compression and shear distortions of intermolecular bonds projected into the ab plane (with respective force constants $K_{\perp 1}$ and $K_{\perp 2}$), and shear distortions of bonds projected onto the c-axis (force constant K_{\parallel}). The thermal diffuse scattering intensity was then refined against the thermal diffuse scattering data in the hk0, hk1, hk2, and h0l planes, with the three force constants that enter into the dispersion realtions (see Appendix B) free to vary. The number of unit cells in the sample was estimated to be 4.8×10^{15} , and the incident flux was taken to be 1×10^9 . In this case, values of $K_{\perp 1} = 22.9(4) \text{ Nm}^{-1}$, $K_{\perp 2} = 5.9(1) \text{ Nm}^{-1}$, and $K_{\parallel} = 7.3(1) \text{ Nm}^{-1}$ were obtained. We note, however, that the flux value is strongly correlated with the average amplitude of the above force constants, and its value was chosen to give phonon dispersions in the typical range $\sim 1 - 10$ THz. Hence, the absolute values of these force constants should be taken lightly. However, the qualitative agreement between calculation and experimental data is excellent (Figure 2). While the true phonon spectrum is far more complex, our rigid-body analysis strongly supports the expectation that crystallisation of this material is based on weakly interacting coordination complexes, and that the chemical interactions between units, including X···X pathways, are weak compared to intra-molecular bonds.

3.3. Charge density and bonding analysis

The experimental structures obtained from HAR refinement were used to perform density functional theory calculations of the electron density distribution in $Ni_2X_4(3,5\text{-lutidine})_8$ and $Ni_2(HF_2)_3(pyrazine)_8$ clusters. These clusters contain the first coordination sphere of Ni^{2+} , with the respective magnetic exchange pathways shown schematically in Figure 3, and as HOMO orbitals for each halide species in Figure 6 of Appendix A. Quantum theory of atoms in molecules (QTAIM) [27] was used to provide a description of the chemical bonding based on the topological analysis of the calculated electron density (see

Table 2), which can then be used to identify changes introduced by different halides and the molecular ligand HF₂⁻.

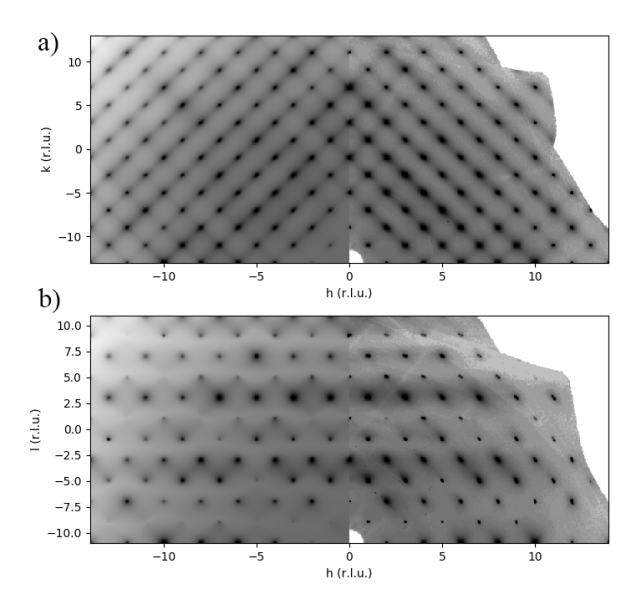


Figure 2
Thermal diffuse scattering measured (right) and calculated (left) in the a) *hk*0 and b) *h0l* reciprocal lattice planes at 300 K.

The bond critical point (bcp) is defined as the point between two atoms where the gradient of the electron density is minimal in the direction of the bond, and maximal in directions perpendicular to the bond. The properties of the electron density at these points characterise the bond, and therefore reflect the type of interaction. We found that the electron density, ρ , at the metal-ligand bcps is the same order of magnitude for both metal-halide and metal-nitrogen interactions, the latter being the larger of the two and similar across all materials (Table 2). The electron density, ρ at the Ni-X bcps is also similar for all materials, with a monotonic decrease with increasing bond length (I→Cl). All metal-ligand interactions have a positive value of the Laplacian, $\nabla^2 \rho$, indicating a depletion of charge at the bcp, as is found for coordinative interactions. The interactions within the molecular ligands, as shown in the Table 2 by the N-C, C-H, C-C and F-H entries, have values of ρ that are nearly an order of magnitude larger than those observed in the metal-ligand bonds. These values indicate charge accumulation at the bcps, as confirmed by the negative values of the Laplacian.

Compared to all other bonds, the X-X interactions in $[NiX_2(3,5\text{-lutidine})_4]$ show very small values of ρ (\sim 0 for X = Cl) and a very flat charge distribution. However, there occurs an increase in ρ of over an order of magnitude on substituting iodine for chlorine, indicating the onset of weak chemical interactions. Bonding parameters based on the experimental charge-density analysis of $[NiI_2(3,5\text{-lutidine})_4]$ (summarised in Figure 5 of Appendix A) are also given in Table 2. The values for charge density are in excellent agreement with those calculated above. The signs and general trends of the Laplacian are also consistent, but the experimental amplitudes were found

to be larger. This is likely due to the acute sensitivity of the Laplacian amplitude to the structural geometry, as it depends inversely on the 5th power of distance, while the charge density depends inversely on the 3rd power.

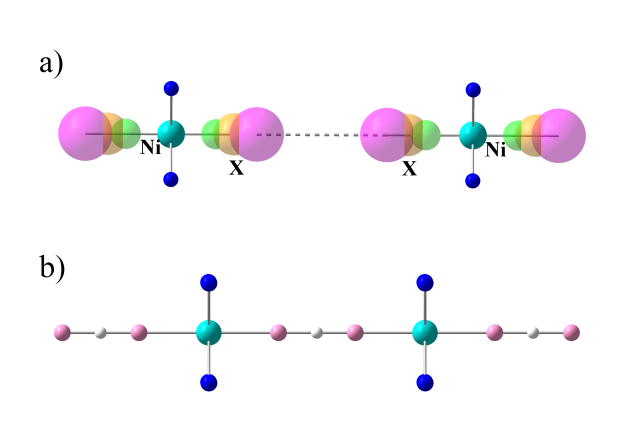


Figure 3 The magnetic exchange interaction pathways of a) $[NiX_2(3,5-lutidine)_4]$ and b) $[NiHF_2(pyrazine)_2]SbF_6$. X = Cl, Br, and I anions are superposed in (c) using green, yellow, and purple spheres, respectively.

The wavefunction obtained in the calculation of the electron density allows one to derive the delocalisation index (DI) for each interacting pair of atoms by integrating the probability density in the atomic regions. The DI is a measure of the electrons shared between two atoms and as such provides an estimate of the covalent character of their interaction and bond order [30]. The C-C and C-N bonds in the aromatic rings are classical examples of covalent interactions, and we find consistent DI values of \sim 1e. Here, the DI confirms the similar electronic properties of lutidine and pyrazine ligands. The covalency of all Ni-N and Ni-X interactions is similar, except for Ni-F which was found to be significantly smaller and close to that of the F-H interaction in the HF₂ molecular ligands. While the $X \cdots X$ interactions are expected to be dominated by Van der Waals forces, the trend in DI values from \sim 0 to \sim 0.1 e by substituting chlorine for iodine indicates the onset of weak covalency.

The integrated charges within the atomic basis defined by the gradient of the electron density are given in Table 3. The charges of the organic ligands are consistent with their expected neutrality, however the charges of the cations and anions show a considerable departure from their formal ionic charges indicating the important role of covalency in the magnetic exchange pathways. Indeed, of all the anions the calculated charge of iodine deviates the most from its formal charge of -1.

Table 2

Bond analysis parameters for [NiX₂(3,5-lutidine)₄] and [NiHF₂(pyrazine)₂]SbF₆ obtained using the quantum theory of atoms in molecules. The asterisk indicates that the X-X data corresponds to a F-H bond. Charge-density, ρ , and the Laplacian, $\nabla^2 \rho$ are given in units e.Bohr⁻³ and e.Bohr⁻⁵, respectively.

		DFT			Exp.
ρ	NiHF ₂ (pyz) ₂ SbF ₆	NiCl ₂ lut ₄	NiBr ₂ lut ₄	NiI2lut4	NiI ₂ lut ₄
X-X	0.1762*	0.0003	0.0011	0.0047	0.004(0)
Ni-X	0.0487	0.0474	0.0406	0.0364	0.031(0)
Ni-N	0.0679	0.0637	0.0641	0.0643	0.061(1)
N-C	0.3367	0.3378	0.3379	0.3312	0.348(3)
C-H	0.3009	0.3026	0.3054	0.2946	0.287(6)
C-C	0.3209	0.3129	0.3136	0.3112	0.321(3)
$\nabla^2 \rho$					Ī
X-X	-0.1173*	0.0002	0.0005	0.0028	0.010(0)
Ni-X	0.0806	0.0327	0.021	0.0144	0.094(0)
Ni-N	0.0782	0.0734	0.0737	0.0615	0.276(0)
N-C	-0.2628	-0.2656	-0.2654	-0.2188	-0.904(3)
C-H	-0.2951	-0.2968	-0.3022	-0.2649	-0.751(5)
C-C	-0.2376	-0.2222	-0.2234	-0.2177	-0.772(2)
DI [e]					<u> </u>
X-X	0.249*	0.004	0.019	0.096	-
Ni-X	0.241	0.402	0.407	0.414	-
Ni-N	0.380	0.366	0.373	0.366	-
N-C	1.288	1.285	1.283	1.247	-
C-H	0.898	0.899	0.898	0.892	-
C-C	1.297	1.321	1.321	1.321	-

Table 3

Integrated charges within the atomic basis defined by the gradient of the electron density for $[NiX_2(3,5-lutidine)_4]$ and $[NiHF_2(pyrazine)_2]SbF_6$, obtained using the quantum theory of atoms in molecules.

Q	NiHF ₂ (pyz) ₂ SbF ₆	NiCl ₂ lut ₄	NiBr ₂ lut ₄	NiI ₂ lut ₄
Ni ²⁺	1.318	1.19	1.15	1.06
X^-/HF_2^-	-0.88	-0.74	-0.71	-0.67
pyz/lut -	0.13	0.06	0.08	0.06

3.4. Spin density and magnetic exchange

Here, we verify that the experimental geometries obtained from HAR refinement, used above to analyse chemical bonding, could be used to reproduce the experimental trends in the Heisenberg exchange coefficients of the Ni^{2+} - $X \cdot \cdot \cdot X$ - Ni^{2+} and Ni²⁺-FHF-Ni²⁺ pathways. The coefficients were obtained from the energy difference of the FM and AFM spin configurations, as described in Section 2. Table 4 reports the calculated values, which are in very good agreement with those found experimentally. It is perhaps surprising that the Ni²⁺-I··· I-Ni²⁺ and Ni²⁺-FHF-Ni²⁺ pathways mediate a similar magnitude of exchange. To understand this coincidence further, we used our calculations to obtain the spin density localised on the magnetic Ni²⁺ ions, and delocalised on the binding atoms of the ligands (Table 4 and Figure 7 of Appendix A). The amount of spin density delocalised onto equatorial nitrogen ligands is remarkably constant across the series. The F⁻ ions of the F-H-F molecular ligands carry very little delocalised spin density, while the halide ions in [NiX₂(3,5-lutidine)₄] host significant delocalised spin density that increases monotonically on substituting chlorine,

for bromine and then iodine. These results indicate stronger magnetic interactions between Ni²⁺ and the halide ligands in [NiX₂(3,5-lutidine)₄] compared to [NiHF₂(pyrazine)₂]SbF₆, which we suggest is due to the reduced electron density at the X···X bond centre (characteristic of the through space interaction), which in turn supports a larger overlap with the magnetic transition-metal orbitals. This effect compensates for the apparent lack of orbital overlap in the through space interaction compared to the Ni²⁺-FHF-Ni²⁺ system, and implies that very large interactions may be possible in other materials that host X···X interactions.

Table 4
Exchange coupling constants and spin density, calculated using density functional theory, and evaluated local to Ni²⁺ cations and delocalised on the bonding atoms of its ligands.

	$NiHF_2(pyz)_2SbF_6$	NiCl ₂ lut ₄	NiBr ₂ lut ₄	NiI ₂ lut ₄
J (K)	12.18	0.12	1.09	15.60
Ni^{2+}	85.9 %	82.8 %	81.6 %	79.7 %
X^-	0.7 %	3.4 %	4.0 %	4.9 %
N	2.8 %	2.7 %	2.7 %	2.6 %

4. Conclusions

In summary, we have established highly accurate crystal structure parameters for $[NiX_2(3,5-lutidine)_4]$, with X = Cl, Br, and I, based on HAR analysis of synchrotron X-ray diffraction data. These parameters have then been used in density functional theory calculations of charge and spin density, which have been corroborated by empirical charge-density analysis of the iodine compound. Our results provide evidence for the development of weak halide · · · halide covalency in the iodine system, in which significant magnetic exchange along Ni²⁺-I··· I- Ni²⁺ chains has been reported. We find a largely depleted electron density at the halide · · · halide bond centre, and we propose that remarkably strong through-space magnetic exchange interactions in coordination polymers can occur when the exchange pathway is 'switched-on' by very weak covalency, enhanced by a charge density that is naturally localised on the ligand's atoms that bond to the magnetic metal ions.

5. Acknowledgements

We acknowledge ARCHER2 UK National Computing Service for computational resourses via HPC-CONEXS under EPSRC grant no. EP/X035514/1 and STFC Scientific Computing Department's SCARF cluster. We acknowledge Diamond Light Source for time on Beamline I19 under Proposal CY30375.

Appendix A Crystallographic data, refinement details and electron density analysis

In Table 1 we report the complete run list used to collect single-crystal diffraction data on beamline I19 (Experimental

hutch 1) at Diamond Light Source. Crystallographic data and agreement factors for independent atom model (IAM), Hirshfeld atom model (HAR) and Hansen–Coppens multipolar model (MM) are given in Table 2 and Table 3.

Table 1

Data collection run list for beamline I19 (Experimental hutch 1) at Diamond Light Source for detector distance 160 mm.

ω/ϕ rotation	ω/φ (°)	2θ (°)	Axis start (°)	Axis end (°)	step (°)
ϕ	0.0	0.0	0.0	360.0	0.1
ω	0.0	25.0	-150.0	20.0	0.1
ω	120.0	25.0	-150.0	20.0	0.1
ω	240.0	25.0	-150.0	20.0	0.1
ω	0.0	45.0	-130.0	40.0	0.1
ω	60.0	45.0	-130.0	40.0	0.1
ω	120.0	45.0	-130.0	40.0	0.1
ω	180.0	45.0	-130.0	40.0	0.1
ω	240.0	45.0	-130.0	40.0	0.1
ω	300.0	45.0	-130.0	40.0	0.1
ω	0.0	65.0	-110.0	60.0	0.1
ω	120.0	65.0	-110.0	60.0	0.1
ω	240.0	65.0	-110.0	60.0	0.1
ω	0.0	85.0	-90.0	80.0	0.1
ω	60.0	85.0	-90.0	80.0	0.1
ω	120.0	85.0	-90.0	80.0	0.1
ω	180.0	85.0	-90.0	80.0	0.1
ω	240.0	85.0	-90.0	80.0	0.1
ω	300.0	85.0	-90.0	80.0	0.1

Table 2
Crystallographic data collected at 100 K, lattice parameters and agreement factors for refinemnt of independent atom model (IAM) and Hirshfeld atom model (HAR) on [NiHF2(pyrazine)] SbFs, and [NiCl3(3.5-lutidine)].

(HAR) on [NiHF ₂ (pyrazine) ₂		· -
	$[NiHF_2(pyrazine)_2]SbF_6$	$[NiCl_2(3,5-lutidine)_4]$
empirical formula	$NiSbF_{10}N_5C_{10}H_{11}$	$NiCl_2N_4C_{28}H_{36}$
formula weight (g/mol ¹)	571.66	558.21
symmetry	tetragonal	tetragonal
space group, Z	P4/nmm, 8	P4/nnc, 8
a,b(Å)	9.9063(1)	11.5371(1)
c (Å)	6.4357(1)	10.5513(1)
volume (Å ³)	631.57(1)	1404.43(3)
F(000)	471.1	589.5
2θ range (deg)	5.6 - 48.8	4.8 - 70.1
index ranges	$-23 \le h \le 24$	$-28 \le h \le 28$
	$-24 \le k \le 24$	$-22 \le k \le 21$
	$-15 \le 1 \le 15$	$-16 \le 1 \le 26$
reflections(unique)	106972(889)	109001(1711)
R _{int}	0.0836	0.0621
I/sigma	65.7	70.8
IAM ref	finement up to 0.6 Å resolution	on
data/parameters	889/38	1711/44
GooF on F ²	1.04	1.00
R ₁ [all data](%)	1.18	2.80
wR ₂ [all data] (%)	3.31	7.72
largest diff peak/hole (e/Å ³)	0.6/-0.4	0.6/-0.5
HAR re	finement up to 0.6 Å resoluti	on
GooF on F ²	-	1.05
R ₁ [all data](%)	-	1.12
wR ₂ [all data] (%)	-	2.67
largest diff peak/hole (e/Å ³)	-	0.4/-0.3

Table 3

Crystallographic data collected at $100\,\mathrm{K}$, lattice parameters and agreement factors for refinement of independent atom model (IAM) and Hirshfeld atom model (HAR) on [NiBr₂(3,5-lutidine)₄] and [NiI₂(3,5-lutidine)₄], and the Hansen–Coppens multipolar model (MM) on [NiI₂(3,5-lutidine)₄] only.

	[NiBr ₂ (3,5-lutidine) ₄]	[NiI ₂ (3,5-lutidine) ₄]
empirical formula	$NiBr_2N_4C_{28}H_{36}$	$NiI_2N_4C_{28}H_{36}$
formula weight (g/mol ¹)	647.11	741.11
symmetry	tetragonal	tetragonal
space group, Z	P4/nnc, 8	P4/nnc, 8
a,b(Å)	11.7571(1)	12.0231(1)
c (Å)	10.1909(1)	9.9896(1)
volume (Å ³)	1408.68(2)	1444.04(1)
F(000)	652.5	731.1
2θ range (deg)	4.7 - 70.0	4.6 - 70.1
index ranges	$-22 \le h \le 20$	$-29 \le h \le 29$
	$-21 \le k \le 22$	$-28 \le k \le 29$
	$-19 \le 1 \le 19$	$-24 \le 1 \le 24$
reflections(unique)	75665(1718)	236805(1764)
Rint	0.0496	0.0556
I/sigma	80.6	108.6
IAM refin	ement up to 0.6 Å resoluti	on
data/parameters	1718/66	1764/44
GooF on F ²	0.98	1.01
R ₁ [all data](%)	1.90	1.27
wR_2 [all data] (%)	6.12	3.57
largest diff peak/hole (e/Å ³)	1.1/-0.5	0.7/-0.5
	ement up to 0.6 Å resoluti	on
GooF on F ²	0.95	1.04
R ₁ [all data](%)	1.65	0.78
wR_2 [all data] (%)	5.61	1.96
largest diff peak/hole (e/Å ³)	1.1/-0.5	0.3/-0.4
	refinement up to 0.45 Å	
GooFw on F ²	-	0.93
R ₁ [all data](%)	-	1.25
wR ₂ [all data] (%)	-	2.60
largest diff peak/hole (e/Å ³)	-	0.34/-0.6

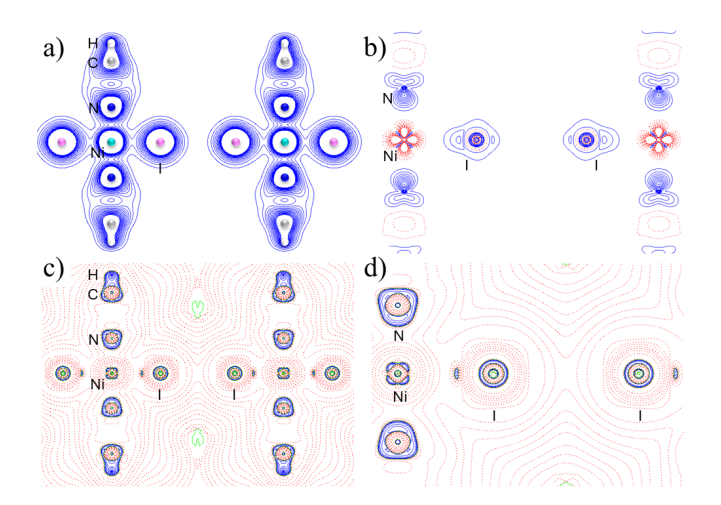


Figure 5 Results from the MM in terms of a) charge density distribution at the 0.1 eÅ^{-3} contour level, b) static deformation density at the 0.2 eÅ^{-3} contour level where blue and red represent, respectively, the excess and depletion of electron density

the Ni-I··· I region.

blue and red represent, respectively, the excess and depletion of electron density with respect to the spherical atom distribution, c) Laplacian function of the charge density with positives contours drawn as solid blue lines indicating regions of charge concentration and negative contours shown as red dotted lines highlighting regions of charge depletion with contours at $\pm 2.0\cdot 10n$, $\pm 4.0\cdot 10n$ and $\pm 8.0\cdot 10n$ (n = -2, -1, 0, +1)eÅ^-5, and d) highlight of the the Laplacian in

a)
b)
c)

Figure 6 Highest occupied molecular orbital shown at contour level $0.03 \, e/\mathring{A}^3$ for a) [NiCl₂(3,5-lutidine)₄], b) [NiBr₂(3,5-lutidine)₄] and c) [NiI₂(3,5-lutidine)₄] as obtained from the Gaussian16 calculations.

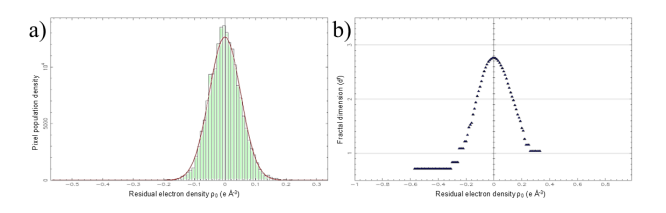


Figure 4 a) Residual density distribution and b) fractal dimension analysis after the MM refinement for $[NiI_2(3,5-lutidine)_4]$.

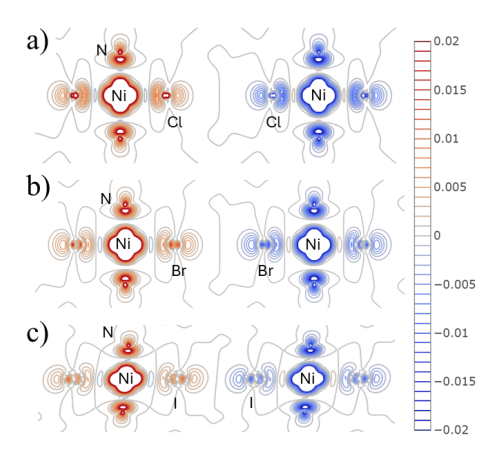


Figure 7 Electron spin-density distribution calculated with Crystal23 for the AFM configuration in a) [NiCl₂(3,5-lutidine)₄], b) [NiBr₂(3,5-lutidine)₄] and c) [NiI₂(3,5-lutidine)₄] and shown between ± 0.02 e/Å³ with 0.001 step size.

Appendix B

Thermal diffuse scattering calculations

We begin by calculating the phonon dispersion. The eigenvalue equation to be solved is

$$D\mathbf{e}_i = \boldsymbol{\omega}_i^2(\mathbf{k})\mathbf{e}_i \tag{2}$$

where D is the dynamical matrix for nearest neighbour interactions between NiX₂lut₄ molecular units, and ω_i^2 is the squared **k**-dependent dispersion of the i^{th} phonon eigenmode, \mathbf{e}_i . We have two molecules in the unit cell, each with 3 degrees of freedom corresponding to displacements along x, y, and z (see Figure 8). Hence, we anticipate 6 eigenmodes; 3 acoustic and 3 optic phonons. The elements of the dynamical matrix can be calculated using the expression

$$D_{j,j'}^{\eta,\eta'}(\mathbf{k}) = \frac{1}{m} \sum_{n'} \Phi_{j,n,j',n'} \exp(-i\mathbf{k} \cdot (\mathbf{r}_{j'n'} - \mathbf{r}_{jn}))$$
(3)

where m is the mass of a molecular unit, and j and j' are nearest neighbour molecules in unit cells n and n', respectively, separated by the vector $(\mathbf{r}_{j'n'} - \mathbf{r}_{jn})$ [31]. It is sufficient to consider only nearest neighbour interactions of the two molecules (labelled 1 and 2) in the zeroth unit cell. Hence, in the following we can set n = 0, j = 1, 2, j' = 1, 2, and n' runs over the neighbouring unit cells 1 to 14, as shown in Figure 8.

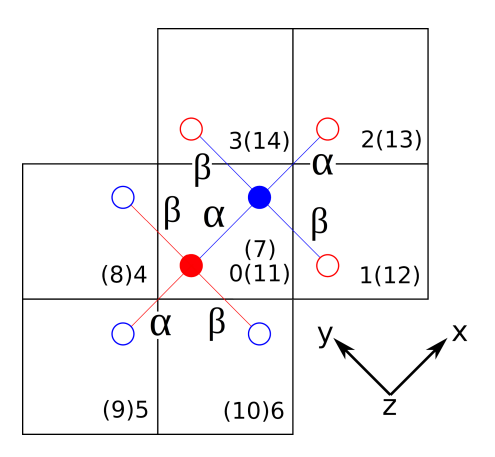


Figure 8

The nearest neighbour interactions included in the calculation of the dynamical matrix. Site 1 is red, site 2 is blue. Unit cells indexed 0-6 lie in the zeroth *ab* plane. Cells indexed 7-10 lie below the zeroth plane, and those indexed 11-14 lie above.

 $\Phi_{j,n,j',n'}$ is the differential of the total energy with respect to the atomic displacements of molecules (n,j) and (n',j') along a given direction (we will assume zero coupling between orthogonal displacements). It can be shown that

$$\Phi_{j,0,j',n'} = -\phi_{j,0,j',n'} + \delta_{j,j'}\delta_{0,n'} \sum_{k' \ m'} \phi_{j,0,k',m'}$$
 (4)

where $\phi_{j,0,j',n'}$ is the differential of an individual bond energy associated with the relative displacements of molecules (0,j) and (n',j').

It is convenient to identify 2 different types of nearest neighbour bonds, labelled α and β in Figure 8. When projected into the ab plane the α and β bonds are aligned along x and y, respectively. In this case Equation 4 yields

$$\Phi_{1,0,1,0} = \Phi_{2,0,2,0} = 4(\phi_{\alpha} + \phi_{\beta}) \tag{5}$$

$$\Phi_{1,0,2,0} = \Phi_{1,0,2,9} = \Phi_{1,0,2,5} = \Phi_{1,0,2,7} = -\phi_{\alpha}$$
 (6)

$$\Phi_{1,0,2,4} = \Phi_{1,0,2,10} = \Phi_{1,0,2,6} = \Phi_{1,0,2,8} = -\phi_{\beta}$$
 (7)

$$\Phi_{2,0,1,0} = \Phi_{2,0,1,13} = \Phi_{2,0,1,2} = \Phi_{2,0,1,11} = -\phi_{\alpha}$$
 (8)

$$\Phi_{2,0,1,1} = \Phi_{2,0,1,14} = \Phi_{2,0,1,3} = \Phi_{2,0,1,12} = -\phi_{\beta} \quad (9)$$

where ϕ depend only on bond type.

We now consider parallel displacements in the three orthogonal directions x, y, and z. For displacements along x, the α bonds are stretched and compressed, while the β bonds are in shear. We associate the former bond distortion with a force constant $\phi_{\alpha}=K_{\perp 1}$, and the latter distortion with a force constant $\phi_{\beta}=K_{\perp 2}$. The opposite is true for displacements along y, *i.e.* $\phi_{\alpha}=K_{\perp 2}$ and $\phi_{\beta}=K_{\perp 1}$. Displacements along z have all bonds in shear, giving $\phi_{\alpha}=\phi_{\beta}=K_{\parallel}$. The dynamical matrix can then be written

$$D = \frac{4}{m} \begin{pmatrix} a & 0 & 0 & -c & 0 & 0 \\ 0 & a & 0 & 0 & -d & 0 \\ 0 & 0 & b & 0 & 0 & -e \\ -c & 0 & 0 & a & 0 & 0 \\ 0 & -d & 0 & 0 & a & 0 \\ 0 & 0 & -e & 0 & 0 & b \end{pmatrix}$$
(10)

defined in the basis $(e_1^x, e_1^y, e_1^z, e_2^x, e_2^y, e_2^z)$, where

$$a = K_{\perp 1} + K_{\perp 2} \tag{11}$$

$$b = 2K_{\parallel} \tag{12}$$

$$c = \cos(\pi l) (K_{\perp 1} \cos(\pi (h+k)) + K_{\perp 2} \cos(\pi (h-k)))$$

$$d = \cos(\pi l) (K_{\perp 2} \cos(\pi (h+k)) + K_{\perp 1} \cos(\pi (h-k)))$$
(14)

$$e = 2\cos(\pi l)K_{\parallel}\cos(\pi h)\cos(\pi k) \tag{15}$$

Diagonalisation of D then gives the eigenmodes

$$\mathbf{e}_1 = (-1, 0, 0, 1, 0, 0) \tag{16}$$

$$\mathbf{e}_2 = (1, 0, 0, 1, 0, 0) \tag{17}$$

$$\mathbf{e}_3 = (0, -1, 0, 0, 1, 0) \tag{18}$$

$$\mathbf{e}_4 = (0, 1, 0, 0, 1, 0) \tag{19}$$

$$\mathbf{e}_5 = (0, 0, -1, 0, 0, 1) \tag{20}$$

$$\mathbf{e}_6 = (0, 0, 1, 0, 0, 1) \tag{21}$$

which correspond to acoustic modes with displacements along x, y, and z (\mathbf{e}_2 , \mathbf{e}_4 , and \mathbf{e}_6 , respectively) and optic modes with displacements along x, y, and z (\mathbf{e}_1 , \mathbf{e}_3 , and \mathbf{e}_5 , respectively). The eigenvalues are

$$\omega_1^2 = \frac{4}{m} (K_{\perp 1} (1 + \cos(\pi (h + k)) \cos(\pi l)) + K_{\perp 2} (1 + \cos(\pi (h - k)) \cos(\pi l))$$
(22)

$$\omega_2^2 = \frac{4}{m} (K_{\perp 1} (1 - \cos(\pi (h + k)) \cos(\pi l)))$$

+
$$K_{\perp 2}(1 - \cos(\pi(h - k))\cos(\pi l))$$
 (23)

$$\omega_3^2 = \frac{4}{m} (K_{\perp 2} (1 + \cos(\pi (h + k)) \cos(\pi l)))$$

+
$$K_{\perp 1}(1 + \cos(\pi(h-k))\cos(\pi l))$$
 (24)

$$\omega_4^2 = \frac{4}{m} (K_{\perp 2} (1 - \cos(\pi (h + k)) \cos(\pi l)))$$

+
$$K_{\perp 1}(1 - \cos(\pi(h - k))\cos(\pi l))$$
 (25)

$$\omega_5^2 = \frac{8}{m} K_{\parallel} (1 + \cos(\pi h) \cos(\pi k) \cos(\pi l)) \qquad (26)$$

$$\omega_6^2 = \frac{8}{m} K_{\parallel} (1 - \cos(\pi h) \cos(\pi k) \cos(\pi l)) \qquad (27)$$

The thermal diffuse scattering intensity is

$$I = \frac{N\hbar}{2} \sum_{i} \frac{1}{\omega_{i}(\mathbf{k})} \coth\left(\frac{\hbar\omega_{i}(\mathbf{k})}{2k_{B}T}\right) |F_{i}(\mathbf{Q})|^{2}$$
 (28)

where N is the number of unit cells in the sample, i labels the phonon modes, and

$$F_i(\mathbf{Q}) = \sum_j \frac{1}{\sqrt{m}} f_j(\mathbf{Q}) [\mathbf{Q} \cdot \mathbf{e}_{i,j}] e^{-\langle u_j \rangle^2 Q^2 / 3}$$
 (29)

where $f_j(\mathbf{Q})$ is the molecular form factor and $e^{-\langle u_j \rangle^2 Q^2/3}$ is the Debye-Waller factor [32]. The sum is taken over the two molecules in the unit cell; j = 1, 2. We note that this expression

is often given with an additional factor $\exp[i\mathbf{Q} \cdot \mathbf{r}_j]$. Whether or not this factor should be included depends on the definition of dynamical matrix.

A value of $\langle u_j \rangle^2 = 0.07 \text{ Å}^2$ was estimated based on atomic displacement parameters refined against Bragg intensities measured at 300 K. Similarly, in the calculation of $f_j(\mathbf{Q})$ fractional coordinates and lattice parameters refined against Bragg intensities were used.

Equation 28 was simplified by taking the first two terms in the Taylor expansion of coth(x) about zero. This serves as a good approximation for moderate to high temperatures, and gives

$$I = Nk_B T \sum_{i} \left(\frac{1}{\omega_i^2} + \frac{1}{12} \left(\frac{\hbar}{k_B T} \right)^2 \right) |F_i(\mathbf{Q})|^2$$
 (30)

The incident flux, Φ , and classical electron radius, r_0 , were added as prefactors to achieve the correct units for I, while experimental factors such as absorption and detector efficiency were ignored. The thermal diffuse scattering intensity was then calculated for the acoustic phonon modes only, with 3 free parameters, $K_{\perp 1}$, $K_{\perp 2}$, K_{\parallel} , which enter into the dispersion relations, ω_i . $N=4.8\times 10^{15}$ was estimated based on the sample size, and the incident flux was taken to be 1×10^9 . The flux value is strongly correlated with the average amplitude of the above force constants. Its value was chosen to give phonon dispersions in the typical range $\sim 1-10$ THz.

A background of the form

$$I_{bkgd} = A \frac{\sin^2(wQ)}{(wQ)^2} \tag{31}$$

was added, where A and w were free parameters. A slight Gaussian broadening of the calculated thermal diffuse scattering was included, where the Gaussian width was free to vary, and a range mask was applied to both data and calculation to 'punchout' Bragg intensities.

The values $K_{\perp 1} = 22.9(4) \text{ Nm}^{-1}$, $K_{\perp 2} = 5.9(1) \text{ Nm}^{-1}$, and $K_{\parallel} = 7.3(1) \text{ Nm}^{-1}$ were refined against the thermal diffuse scattering data in the hk0, hk1, hk2, and h0l planes. In each case reciprocal space slices were taken with a thickness of ± 0.25 reciprocal lattice units, and the fitting results are shown in Figures 2 and 9.

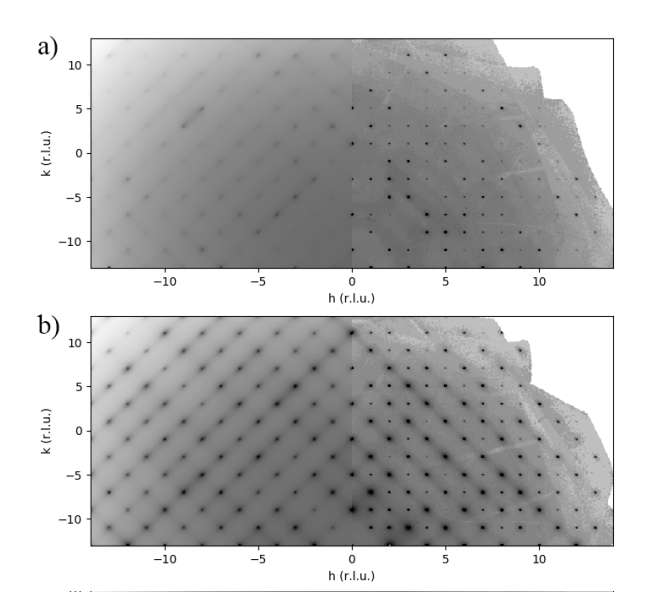


Figure 9 Thermal diffuse scattering measured (right) and calculated (left) in the a) hk1 and b) hk2 reciprocal lattice planes at 300 K.

References

- [1] Jamie L. Manson, Zachary E. Manson, Ashley Sargent, Danielle Y. Villa, Nicole L. Etten, William J.A. Blackmore, Samuel P.M. Curley, Robert C. Williams, Jamie Brambleby, Paul A. Goddard, Andrew Ozarowski, Murray N. Wilson, Benjamin M. Huddart, Tom Lancaster, Roger D. Johnson, Stephen J. Blundell, Jesper Bendix, Kraig A. Wheeler, Saul H. Lapidus, Fan Xiao, Serena Birnbaum, and John Singleton. Enhancing easyplane anisotropy in bespoke ni(ii) quantum magnets. *Polyhedron*, 180:114379, 2020.
- [2] Panagiota Perlepe, Itziar Oyarzabal, Aaron Mailman, Morgane Yquel, Mikhail Platunov, Iurii Dovgaliuk, Mathieu Rouzières, Philippe Négrier, Denise Mondieig, Elizaveta A Suturina, et al. Metal-organic magnets with large coercivity and ordering temperatures up to 242 c. *Science*, 370(6516):587–592, 2020.
- [3] Xiang Li, Dong Zhang, Yuqing Qian, Wenxuan Liu, Corine Mathonière, Rodolphe Clérac, and Xin Bao. Chemical manipulation of the spin-crossover dynamics through judicious metalion dilution. *Journal of the American Chemical Society*, 145(17):9564–9570, 2023.
- [4] Rebecca Scatena, Roger D Johnson, Pascal Manuel, and Piero Macchi. Formate-mediated magnetic superexchange in the model hybrid perovskite [(ch 3) 2 nh 2] cu (hcoo) 3. *Journal of Materials Chemistry C*, 8(37):12840–12847, 2020.
- [5] Thomas Bjørn Egede Grønbech, Lennard Krause, Davide Ceresoli, and Bo Brummerstedt Iversen. Elucidating the superexchange mechanisms in magnetic coordination polymer [co (hcoo) 2 (h 2 o) 2]∞ through chemical bonding analysis. *Journal of Materials Chemistry C*, 11(38):12922–12932, 2023.
- [6] Leonardo HR Dos Santos, Arianna Lanza, Alyssa M Barton, Jamie Brambleby, William JA Blackmore, Paul A Goddard, Fan Xiao, Robert C Williams, Tom Lancaster, Francis L Pratt, et al. Experimental and theoretical electron density analysis of copper pyrazine nitrate quasi-low-dimensional quantum magnets. *Jour*nal of the American Chemical Society, 138(7):2280–2291, 2016.

- [7] Mariusz Kubus, Arianna Lanza, Rebecca Scatena, Leonardo HR Dos Santos, Bjørn Wehinger, Nicola Casati, Christoph Fiolka, Lukas Keller, Piero Macchi, Christian Ruegg, et al. Quasi-2d heisenberg antiferromagnets [cux (pyz) 2](bf4) with x= cl and br. *Inorganic chemistry*, 57(9):4934–4943, 2018.
- [8] Jamie L Manson, T Lancaster, LC Chapon, SJ Blundell, JA Schlueter, ML Brooks, FL Pratt, CL Nygren, and JS Qualls. Cu (hco2) 2 (pym)(pym= pyrimidine): low-dimensional magnetic behavior and long-range ordering in a quantum-spin lattice. *Inorganic chemistry*, 44(4):989–995, 2005.
- [9] J Liu, S Kittaka, RD Johnson, T Lancaster, John Singleton, T Sakakibara, Y Kohama, J Van Tol, A Ardavan, BH Williams, et al. Unconventional field-induced spin gap in an s= 1/2 chiral staggered chain. *Physical Review Letters*, 122(5):057207, 2019.
- [10] E. P. Kenny, A. C. Jacko, and B. J. Powell. Tight-binding approach to pyrazine-mediated superexchange in copper-pyrazine antiferromagnets. *Inorganic Chemistry*, 60(16):11907–11914, 2021. PMID: 34310131.
- [11] William J. A. Blackmore, Samuel P. M. Curley, Robert C. Williams, Shroya Vaidya, John Singleton, Serena Birnbaum, Andrew Ozarowski, John A. Schlueter, Yu-Sheng Chen, Beatrice Gillon, Arsen Goukassov, Iurii Kibalin, Danielle Y. Villa, Jacqueline A. Villa, Jamie L. Manson, and Paul A. Goddard. Magnetostructural correlations in ni2+-halide-halide-ni2+ chains. *Inorganic Chemistry*, 61(1):141–153, 2022. PMID: 34939800.
- [12] Robert C. Williams, William J. A. Blackmore, Samuel P. M. Curley, Martin R. Lees, Serena M. Birnbaum, John Singleton, Benjamin M. Huddart, Thomas J. Hicken, Tom Lancaster, Stephen J. Blundell, Fan Xiao, Andrew Ozarowski, Francis L. Pratt, David J. Voneshen, Zurab Guguchia, Christopher Baines, John A. Schlueter, Danielle Y. Villa, Jamie L. Manson, and Paul A. Goddard. Near-ideal molecule-based haldane spin chain. *Phys. Rev. Res.*, 2:013082, Jan 2020.
- [13] Rebecca Scatena, Fabio Montisci, Arianna Lanza, Nicola PM Casati, and Piero Macchi. Magnetic network on demand: Pressure tunes square lattice coordination polymers based on {[Cu (pyrazine) 2] 2+} n. *Inorganic chemistry*, 59(14):10091–10098, 2020.
- [14] Samuel PM Curley, Rebecca Scatena, Robert C Williams, Paul A Goddard, Piero Macchi, Thomas J Hicken, Tom Lancaster, Fan Xiao, Stephen J Blundell, Vivien Zapf, et al. Magnetic ground state of the one-dimensional ferromagnetic chain compounds m (ncs) 2 (thiourea) 2 (m= ni, co). *Physical Review Materials*, 5(3):034401, 2021.
- [15] Jamie Brambleby, Jamie L. Manson, Paul A. Goddard, Matthew B. Stone, Roger D. Johnson, Pascal Manuel, Jacqueline A. Villa, Craig M. Brown, Helen Lu, Shalinee Chikara, Vivien Zapf, Saul H. Lapidus, Rebecca Scatena, Piero Macchi, Yu-sheng Chen, Lai-Chin Wu, and John Singleton. Combining microscopic and macroscopic probes to untangle the single-ion anisotropy and exchange energies in an s = 1 quantum antiferromagnet. Phys. Rev. B, 95:134435, Apr 2017.
- [16] David R Allan, Harriott Nowell, Sarah A Barnett, Mark R Warren, Adrian Wilcox, Jeppe Christensen, Lucy K Saunders, Andrew Peach, Mark T Hooper, Ljubo Zaja, et al. A novel dual air-bearing fixed-χ diffractometer for small-molecule single-crystal x-ray diffraction on beamline i19 at diamond light source. Crystals, 7(11):336, 2017.
- [17] Raw diffraction data are archived by diamond light source, and are available on request from the corresponding author.

10

- [18] G Winter. xia2: an expert system for macromolecular crystallography data reduction. *Journal of applied crystallography*, 43(1):186–190, 2010.
- [19] CrysAlisPRO, Oxford Diffraction / Agilent Technologies UK Ltd, Yarnton, England.
- [20] Oleg V Dolomanov, Luc J Bourhis, Richard J Gildea, Judith AK Howard, and Horst Puschmann. Olex2: a complete structure solution, refinement and analysis program. *Journal of applied crystallography*, 42(2):339–341, 2009.
- [21] Florian Kleemiss, Oleg V Dolomanov, Michael Bodensteiner, Norbert Peyerimhoff, Laura Midgley, Luc J Bourhis, Alessandro Genoni, Lorraine A Malaspina, Dylan Jayatilaka, John L Spencer, et al. Accurate crystal structures and chemical properties from nosphera2. *Chemical Science*, 12(5):1675–1692, 2021.
- [22] Frank Neese, Frank Wennmohs, Ute Becker, and Christoph Riplinger. The orca quantum chemistry program package. *The Journal of chemical physics*, 152(22), 2020.
- [23] N. K. Hansen and P. Coppens. Testing aspherical atom refinements on small-molecule data sets. *Acta Crystallographica Section A*, 34(6):909–921, 1978.
- [24] A Volkov, P Macchi, LJ Farrugia, C Gatti, P Mallinson, R Richter, and T Koritsanszky. A computer program for multipole refinement, topological analysis of charge densities, and evaluation of intermolecular energies from experimental or theoretical structure factors. XD2006 (Version 5.42), 2006.
- [25] P. J. Becker and P. Coppens. Extinction within the limit of validity of the darwin transfer equations. iii. non-spherical crystals

- and anisotropy of extinction. *Acta Crystallographica Section A*, 31(4):417–425, 1975.
- [26] Alessandro Erba, Jacques K Desmarais, Silvia Casassa, Bartolomeo Civalleri, Lorenzo Donà, Ian J Bush, Barry Searle, Lorenzo Maschio, Loredana Edith-Daga, Alessandro Cossard, et al. Crystal23: A program for computational solid state physics and chemistry. *Journal of Chemical Theory and Computation*, 19(20):6891–6932, 2022.
- [27] Richard FW Bader and TT Nguyen-Dang. Quantum theory of atoms in molecules-dalton revisited. In *Advances in quantum chemistry*, volume 14, pages 63–124. Elsevier, 1981.
- [28] TA Keith. Aimall (version 19.10. 12), todd a. keith, tk gristmill software: Overland park ks (2019). *URL: http://aim. tkgristmill. com.*
- [29] Madelyn Smith, Zhen Li, Luke Landry, Kenneth M Merz Jr, and Pengfei Li. Consequences of overfitting the van der waals radii of ions. *Journal of Chemical Theory and Computation*, 19(7):2064– 2074, 2023.
- [30] Alexey I Baranov and Miroslav Kohout. Electron localization and delocalization indices for solids. *Journal of computational chemistry*, 32(10):2064–2076, 2011.
- [31] Dove, M.T. Introduction to the theory of lattice dynamics. *JDN*, 12:123–159, 2011.
- [32] Alexei Bosak and Dmitry Chernyshov. On model-free reconstruction of lattice dynamics from thermal diffuse scattering. *Acta Crystallographica Section A*, 64(5):598–600, Sep 2008.